NANO · MICRO small
www.small-journal.com

# Revealing the Role of Ruthenium on the Performance of P2-Type $Na_{0.67}Mn_{1-x}Ru_xO_2$ Cathodes for Na-Ion Full-Cells

*Emine Altin, Iqra Moeez, Eunji Kwon, Ali Hussain Umar Bhatti, Seungho Yu, Kyung Yoon Chung, Muhammad Arshad, Messaoud Harfouche, Murat Buldu, Sebahat Altundag, Fatih Bulut, Sevda Sahinbay, Serdar Altin,* and Mehmet Nurullah Ates**

**Herein, P2-type layered manganese and ruthenium oxide is synthesized as an outstanding intercalation cathode material for high-energy density Na-ion batteries (NIBs). P2-type sodium deficient transition metal oxide structure, $Na_{0.67}Mn_{1-x}Ru_xO_2$ cathodes where x varied between 0.05 and 0.5 are fabricated. The partially substituted main phase where x = 0.4 exhibits the best electrochemical performance with a discharge capacity of ≈170 mAh $g^{-1}$. The in situ X-ray Absorption Spectroscopy (XAS) and time-resolved X-ray Diffraction (TR-XRD) measurements are performed to elucidate the neighborhood of the local structure and lattice parameters during cycling. X-ray photoelectron spectroscopy (XPS) revealed the oxygen-rich structure when Ru is introduced. Density of States (DOS) calculations revealed the Fermi-Level bandgap increases when Ru is doped, which enhances the electronic conductivity of the cathode. Furthermore, magnetization calculations revealed the presence of stronger Ru—O bonds and the stabilizing effect of Ru-doping on MnO6 octahedra. The results of Time-of-flight secondary-ion mass spectroscopy (TOF-SIMS) revealed that the Ru-doped sample has more sodium and oxygenated-based species on the surface, while the inner layers mainly contain Ru–O and Mn–O species. The full cell study demonstrated the outstanding capacity retention where the cell maintained 70% of its initial capacity at 1 C-rate after 500 cycles.**

## 1. Introduction

The proliferation of electronic devices and, notably, electric vehicles (EVs) has catalyzed significant advancements in electrochemical energy storage systems in recent years. While various types of electrical energy storage systems exist, it is important to highlight the remarkable progress of Li-ion batteries (LIBs) in recent years.[1] The demand for Li-ion batteries has surged, leading to an increase in the consumption of lithium sources.[2] Newly developed electrode materials are expected to possess several key properties, including high energy density, long cycle life, and affordability for commercial feasibility.[3] It is worth noting that LIBs, first introduced by Sony in the 1990s, have become one of the most extensively used battery systems for portable electronics and various other large-scale applications.[4] Recently, there has been significant research into alternative battery types, such as lithium–sulfur (Li–S) and lithium-air (Li-air), to improve the energy density of the current state-of-the-art lithium-ion batteries (LIBs).[5] However, this progress has led to increased costs, primarily due to the limited and unevenly distributed lithium reserves around the globe.[6]

NIBs have appeared as a promising replacement toLIBs because their basic electrochemical properties are similar to LIBs, and they utilize sodium, which is much more abundant and more evenly distributed in the earth than that of lithium.[7] Because of these advantages, NIBs present an environmentally friendly and cost-effective battery option with promising potential to meet the demands of large-scale energy storage, making them a viable alternative to LIBs.[8] In recent years,

E. Altin
Vocational School of Health Service
Inonu University
Battalgazi, Malatya 44280, Türkiye

The ORCID identification number(s) for the author(s) of this article can be found under https://doi.org/10.1002/smll.202406332



**DOI: 10.1002/smll.202406332**

I. Moeez, E. Kwon, A. H. U. Bhatti, S. Yu, K. Y. Chung
Energy Storage Research Center
Korea Institute of Science and Technology
Seongbuk-gu, Seoul 02792, Republic of Korea

A. H. U. Bhatti, K. Y. Chung
Division of Energy and Environment Technology
KIST School
Korea University of Science and Technology
Seoul 02792, Republic of Korea

M. Arshad
Nano-sciences & Technology Department
National Centre for Physics (NCP)
Quaid-i-Azam University (QAU) Campus
Islamabad 44000, Pakistan

several battery companies have emerged with a focus on commercializing sodium-ion cells.[9] It is predicted that sodium-ion battery cells have the potential to swap lithium-ion cells in the near future, given the abundance of sodium and the lower costs associated with it providing a sustainable future for energy storage systems. Therefore, there are significant efforts in R&D activities for new electrode materials used in sodium-ion cells. There are different structural compositions for the Na-ion cathodes such as the layered transition metal oxides,[10] phosphate-based materials,[11] pyrophosphate-based materials,[12] fluorophosphate materials,[13] fluorosilicate-based materials[14] and sulfate-based materials.[15] Manganese-based layered transition metal oxides are among the best materials targeted for the cathode development in sodium-ion batteries. They are gaining attention due to their low cost, high recyclability, and low toxicity.[16] It is known that $Na_xMnO_2$ materials can form 2D layered or 3D tunnel structures, depending on their chemical composition.[17] Most of the $Na_xMnO_2$ structures are classified into P2 and O3 types according to the number of $Na^+$ and $MO_2$ (M = transition metal) layers in the structure.[18] P2-type $Na_xMnO_2$ offers a structural advantage compared to O3-type. In the P2-type, $Na^+$ ions reside within the layers, and the broader rectangular spaces between adjacent layers are elongated. In this structure, Na ions are spread out across the trigonal prismatic regions, resulting in a better dispersion of ions.[19] The most popular P2-type $Na_xMnO_2$ composition can be formulated as $Na_{0.67}Mn_{1-x}TM_xO_2$ (where x = 0–1) where the TMs can be Fe, Cu, Ni, Co, V, or Ti, etc.[20,21] In order to improve battery performance, the combination of the transition elements such as Ni, Cu, Fe, and Mn are among the most preferred elements for the high-performance sodium-containing layered metal oxides. Ruthenium (Ru) has a wide range of valence states when compared with iron in the structure. Considering the electron configuration of Ru, it has only one electron in its outermost shell, which allows it to form coordination complexes with various oxidation states. It has been established that Ru serves as an exceptional catalyst in oxidation reactions, displaying various oxidation states ranging from −2 to +8.[22] The ability of Ru to exist in numerous oxidation states during cycling renders more electrons to be transferred, thereby enhancing battery capacity.

This study successfully fabricated novel P2-type $Na_{0.67}Mn_{1-x}Ru_xO_2$ cathode materials using a modified solid-state reaction technique, and their structural properties were unraveled. It is found that Ru-ions were successfully substituted by Mn-ions in the structure and the highest capacities were obtained for the samples where x = 0.3 and 0.4. In situ XRD and XAS analysis of the cells were conducted to unravel the reaction mechanism of the cells. The full-cell performance of the optimized cell was studied, suggesting that Ru-substituted P2-type cathode materials hold significant potential for Na-ion batteries.

## 2. Results and Discussion

### 2.1. Structural Analysis

The XRD diffraction patterns of the Ru-substituted cathode samples are given in **Figure 1a**. It is seen that the diffraction patterns are well matched by P2-type $P6_3/mmc$ symmetry which is typical Na–Mn–O cathode materials.[23] When the Ru content increased up to x = 0.5, an impurity phase of $Na_2RuO_3$ is observed which has C2/c symmetry. This structure has the following unit parameters; a = 5.4141 Å, b = 9.3663 Å, and c = 10.8481 Å.[24] Figure S2a–f (Supporting Information) displays each XRD pattern for samples doped with different amounts of Ru along with the GSAS refinement fitting results. It is clear that the sample where x = 0.5 exhibits $Na_2RuO_3$ peaks which are shown with the arrow. Nonetheless, the other samples were free of the impurity phase suggesting that the degree of impurity was limited to only the sample where x = 0.5. After the Rietveld-refinement of the samples, the calculated lattice parameters are given in Table S1 (Supporting Information). When examining the a- and c-lattice parameters, it is clear that while the a-lattice parameters remained constant with increasing Ru-content, the c-lattice parameters increased sharply between x = 0.1 and x = 0.2, and then when the value x is further increased, the c-lattice parameter decreased as the Ru-content increased. In addition to this, the Na-layer distance showed a similar trend with the c-parameters of the cells. The right panel of Figure 1a displays the 002 plane, which is directly affected by the c-direction. According to Bragg's law, shifting toward a lower angle in $2\theta$ degrees indicates the crystal lattice expansion. This expansion trend is clearly seen in the peak of the (002) plane in the right panel of Figure 1a from x = 0.05 to x = 0.2. Afterward, the plane position is shifting toward higher angles indicating the shrinkage of the crystal lattice from x = 0.2 until x = 0.5. Overall, the trend in shifting direction of the peak bodes well with the fitting results. To understand the behavior of Ru-ions in the structure, we evaluated the valence state of the Mn-ions in $Na_{0.67}MnO_2$ structure. In this structure, Mn-ions have 3.33+ valence state which means there are different ionic radii of Mn species. These species are speculated to be 0.72 pm low spin (LS) and 0.785 pm high spin (HS) for $Mn^{3+}$ and 0.67 pm for $Mn^{4+}$ existing in the octahedral coordination.[23] Because of this, there is a possibility of having Jahn–Teller active $Mn^{3+}$ ions in the lattice which may cause voltage hysteresis during the sodiation and desodiation process of the battery.[24] On the other hand, the Ru-ions could have three possible different

M. Harfouche
Synchrotron-light for Experimental Science and Applications in the Middle East (SESAME)
Allan 19252, Jordan

M. Buldu, S. Altundag, F. Bulut, S. Altin
Physics Department
Inonu University
Malatya 44280, Türkiye
E-mail: serdar.altin@inonu.edu.tr

S. Sahinbay
Physics Department
Istanbul Technical University
Istanbul 34469, Türkiye

M. N. Ates
Department of Chemistry
Bogazici University
Istanbul 34342, Türkiye
E-mail: mehmet.ates@boun.edu.tr

M. N. Ates
TÜBİTAK Rail Transport Technologies Institute
Energy Storage Division
TÜBİTAK Gebze Campus, Gebze, Kocaeli 41470, Türkiye

 

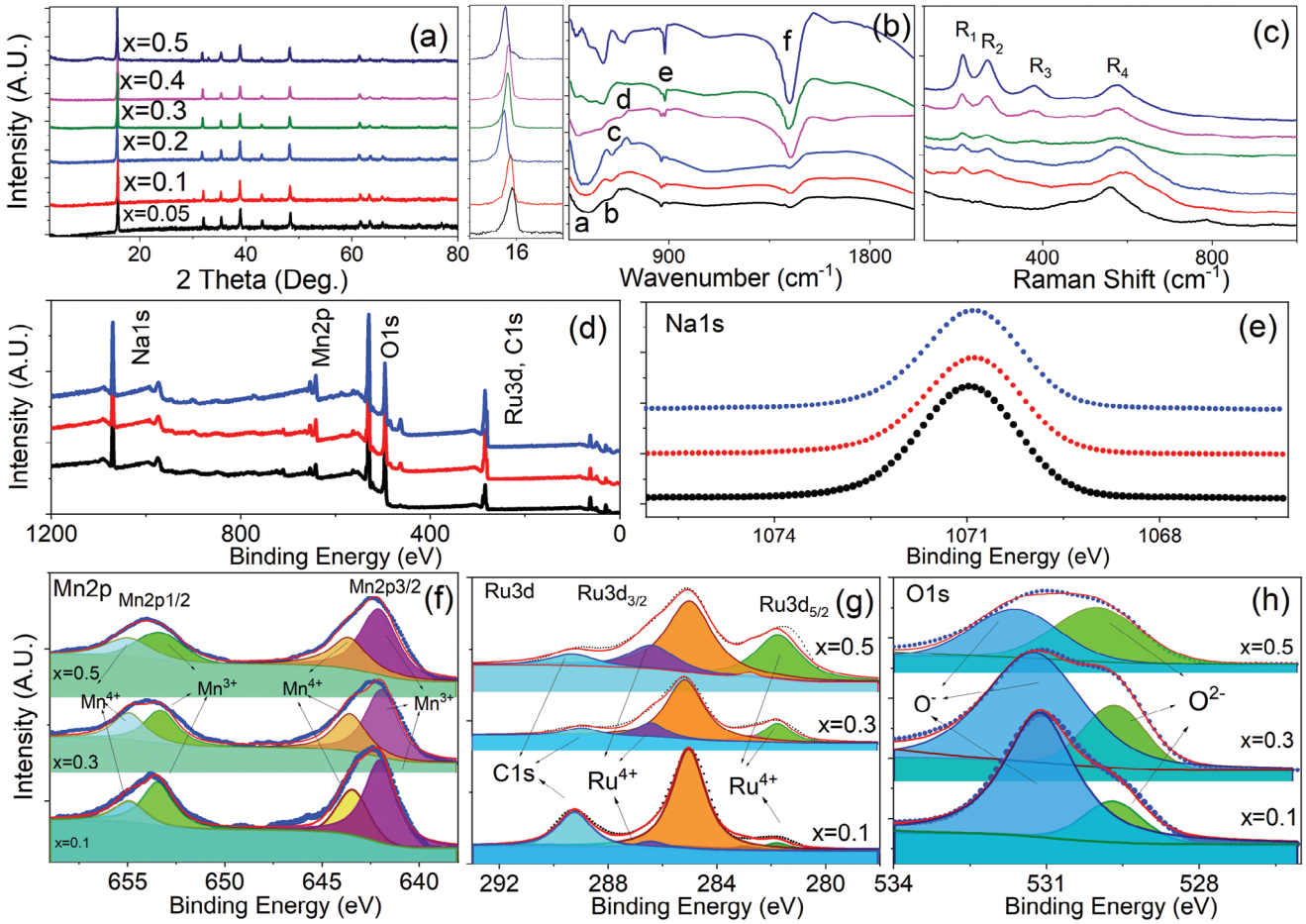


**Figure 1.** a) XRD pattern and right panel shows (002) planes, b) FTIR, c) Raman analysis of the Ru substituted samples of $Na_{0.67}Mn_{1-x}Ru_xO_2$ where x varies between 0.05 and 0.5. d) the Survey data of XPS, e) Na1s, f) Mn2p, g) Ru3d, and h) O1s spectrums for x = 0.1, 0.3, and 0.5 of $Na_{0.67}Mn_{1-x}Ru_xO_2$ Ru substituted powders.

ion radii such as 0.82, 0.76, and 0.705 pm for the valence states of 3+, 4+, and 5+, respectively.[25] It is understood that the XRD peaks are shifted toward the lower angle region when the ion of higher ionic radii substitutes the ion of lower ionic radii due to expansion in the crystal lattice.[26] According to Figure 1a, we observed that the 002 peak shifts to a lower angle up to x = 0.2 and then shifts to a higher angle until x = 0.5. It is anticipated that when ruthenium (Ru) is substituted in low concentrations, the structure has a tendency toward low oxidation states like $Ru^{3+}$ because of its larger ionic radii. However, as the amount of substitution increases, the doped sample is more likely to favor lower ionic radii states, such as $Ru^{4+}$ and $Ru^{5+}$. According to the charge balance of the chemical formula of $Na_{0.67}MnO_2$, there are $Mn^{3+}$ and $Mn^{4+}$ ions in the samples.

When substituting Ru ions with Mn ions, several ion formation possibilities arise in the system: i) the substitution of $Ru^{3+}$ by $Mn^{3+}$, which is feasible for maintaining the charge balance of the system. ii) the substitution of $Ru^{3+}$ by $Mn^{4+}$, which leads to the oxidation of $Mn^{3+}$ to $Mn^{4+}$ in the structure. iii) the substitution of $Ru^{4+}$ by $Mn^{3+}$, resulting in the reduction of $Mn^{4+}$ to $Mn^{3+}$. When considering higher substitutions where x is above 0.2, the (002) peak shifts to higher angles. This shift indicates the substitution of Ru ions with lower ionic radii, such as $Ru^{4+}$ and $Ru^{5+}$, instead of $Ru^{3+}$. When we assume that the $Ru^{5+}$ ions penetrate into the main structure, some of $Mn^{3+}$ or $Mn^{4+}$ ions should transform to $Mn^{2+}$ ions (0.81 for LS and 0.97 for HS) or $Mn^{3+}$ in the structure, respectively. In this case, the lattice volume affects the ionic radii of $Ru^{5+}$ and $Mn^{2+}$ and there should be competition between these ions. When high-valence state Ru ions are present in the structure, maintaining charge balance becomes challenging. As a result, the material tends to absorb more oxygen to achieve charge equilibrium. This increased oxygen absorption can influence various properties of the material, such as its electronic structure and reactivity. We also speculate that due to the high valence state of Ru for the sample where x = 0.5, the structure also forms $Na_2RuO_3$ impurity, shown in the Figure S2f (Supporting Information). We like to note that the valence state of each element will be elaborated in the XPS section.

The FTIR analysis results of the samples are given in Figure 1b and it is observed that the bands at 485 $cm^{-1}$ (assigned as a – bending M–O–M modes of $MO_6$ octahedra), 552 $cm^{-1}$ (assigned b – asymmetric stretching vibrations of $MO_6$ octahedra), 604 $cm^{-1}$ (assigned c – asymmetric stretching vibrations of $MO_6$ octahedra), 703 $cm^{-1}$ (assigned d) which are the characteristic

peaks of $Na_{0.67}MnO_2$ cathode material.[27,28] The FTIR bands at 881 $cm^{-1}$ (assigned e) and 1438 $cm^{-1}$ (assigned f) are related to Ru–O vibration in the structure[29,30] and the absorbance of these two bands was increased by increasing Ru-content in the samples. This trend agrees well with the XRD results where x = 0.5 shows impurity of $Na_2RuO_3$.

The Raman spectrum of the Ru substituted $Na_{0.67}MnO_2$ powders was given in Figure 1c and six different peaks were observed around 214 ($R_1$) $cm^{-1}$, 272 ($R_2$) $cm^{-1}$, 373 ($R_3$) $cm^{-1}$ and 578 ($R_4$) $cm^{-1}$. Posonov et. al. investigated the Raman shift of $Li_2RuO_3$ which is the isostructure of $Na_2RuO_3$ and they claimed that $R_1$ and $R_2$ peaks are related to $A_g$ modes of the C2/m phase.[31] It is well known that the $R_3$ and $R_4$ Raman peaks are related to P2 type $Na_{0.67}MnO_2$.[32] The band around $R_3$ can be explained by the $E_{2g}$ modes in the structure,[33] and the peak at $R_4$ is due to symmetric stretching-mode $A_{1g}$ in the lattice, which is explained by the motions of the oxygen atoms.[34]

Based on the XRD analysis, we can infer that the valence state of transition metals is influenced by the increasing amount of Ru in the materials. This observation suggests that the amount of Ru can affect the oxidation states of other transition metals. To elucidate the change in the valence state of the metal ions in the structure, we performed the XPS analysis of the elements in the samples, and the survey data was presented in Figure 1d. The peaks of C1s, Mn2p, Ru3d, O1s, and Na1s for x = 0.1, 0.3, and 0.5 were observed at ≈280.1, ≈642.1, ≈284.8, ≈530.3, and ≈1070.9 eV, respectively. The Na1s XPS data for x = 0.1, 0.3, and 0.5 in Figure 1e exhibit nearly identical graphs. This similarity indicates that the valence state and crystal field around $Na^+$ ions remain constant albeit with different amount of Ru substitution. This finding aligns with the previous studies on similar compositions.[35] It should be noted that the binding energy difference is called chemical shift and found as 1071.32, 1070.62, and 1070.85 eV for x = 0.1, 0.3, and 0.5, respectively. The positions of peaks can shift because of the chemical properties of nearby atoms and changes in the local environment around the element.[36] It is anticipated that doping the cathode with Ru would alter the local structure of the primary phase. Figure 1f shows the XPS data of the Mn2p for x = 0.1, 0.3, and 0.5 samples suggesting that there are two main peaks of $Mn2p_{3/2}$ and $Mn2p_{1/2}$ which are consisted of $Mn^{3+}$ 641.9 (x = 0.1), 641.9 (x = 0.3), and 642.0 (x = 0.5) eV for $Mn2p_{3/2}$ and 653.4 (x = 0.1), 653.3 (x = 0.3), and 653.4 (x = 0.5) eV for $Mn2p_{1/2}$. In case of $Mn^{4+}$ species, the peaks are located at 643.5 (x = 0.1), 643.6 (x = 0.3) and 643.7 (x = 0.1) eV for $Mn2p_{3/2}$ and 654.9 (x = 0.1), 654.9 (x = 0.3) and 655 (x = 0.5) eV for $Mn2p_{1/2}$ ions. These results are also consistent well with the previous studies.[37] When we calculated the peak area of each of the $Mn^{3+}$ and $Mn^{4+}$ peaks in the XPS data, the ratios of $Mn^{3+}/Mn^{4+}$ ions were calculated as 64.3%/35.7%, 64.5%/35.5%, and 65.3%/34.7% for x = 0.1, 0.3, and 0.5, respectively. When doping with Ru, we expect the average valence state of Ru in the samples to either match the average valence state of Mn or lead to an increase in the number of oxygen ions in the structure. The energy differences between the $2p_{1/2}$ and $2p_{3/2}$ levels correspond to the binding energy separation between the spin-split components which depends on the valence state of the transition metals.[38] While the differences for $Mn^{3+}$ were calculated as 11.5, 11.4, and 11.8 eV for x = 0.1, 0.3, and 0.5, the energy gap for $Mn^{4+}$ was determined as 11.4, 11.3, and 11.3 for x = 0.1, 0.3, and 0.5, respectively. In Figure 1g, we should indicate that the XPS spectrum of Ru3d in samples partially overlaps with the C1s spectrum. The C1s peaks that appeared in the samples are the overlapping of Ru3d spectra positioned at 285 and 289 eV are related to adventitious carbon in the structure.[39] The observed peaks at 281.8, 281.74, and 281.74 eV for x = 0.1, 0.3, and 0.5 are explained by $Ru3d_{5/2}$ of $Ru^{4+}$ ions in the structure which is consistent with the existing studies.[40] We should note that the XPS peak area corresponding to $Ru^{4+}$ ions increased with higher doping levels in the structure. The O1s XPS spectrum of the x = 0.1, 0.3, and 0.5 Ru substituted samples were given in Figure 1h and it is seen that there are two types of oxygen in the structure. The O1s sub-peaks ≈529.6 eV for lower energy region can be explained by Ru—O bond in the sample as described earlier.[39] Although we didn't observe the sub-peaks of oxygen O1s spectrum for P2-type $Na_{0.67}TMO_2$ type cathode materials in our previous studies,[20,21] the second sub-peak of the XPS O1s spectrum is due to $O^{2-}$ metal-oxygen bond in the sodium metal oxide compounds.[40] According to the peak area of these two peaks, the lower energy peak ratios were calculated as 22.9%, 31.7%, and 52.3% for x = 0.1, 0.3, and 0.5, respectively. There are small peak shifts for low energy (529.6, 529.7, and 529.9 eV for x = 0.1, 0.3, and 0.5, respectively) and high energy peaks (531.1, 531.3, and 531.6 eV for x = 0.1, 0.3, and 0.5, respectively) of XPS data. This could be explained by the excess oxygen which implies that there is an electrostatic force effect between Ru and the surrounding oxygen.[39,41]

The BET absorption and desorption graphs are displayed in Figure S3 (Supporting Information) and the obtained shape of the adsorption/desorption curves can be predicted as type IV isotherm which is typical for meso-porous materials.[42] The surface area of the samples was calculated using the data in Figure S3 (Supporting Information) and BET equations and obtained as 1.05, 2.81, 2.28, 1.78, 1.23, and 1.31 $m^2\ g^{-1}$ for x = 0.05, 0.1, 0.2, 0.3, 0.4, and 0.5, respectively. It can be concluded that the surface areas and pore structures of the Ru-doped materials exhibit similar surface properties. This suggests that the Ru dopant does not significantly alter the surface characteristics of the materials. The surface morphology of the Ru-substituted samples, as shown in Figure S4a–f (Supporting Information), reveals similar grain formations characterized by arbitrarily shaped grains with varying geometries and sizes larger than 1 µm. Additionally, the substitution of Ru in the main phase leads to an increase in the size of these grains. This is especially more pronounced in Figure S4e,f (Supporting Information). It is well known that the total free energy change is related to surface-free energy and volume-free energy.[43] As grains grow, the relative contribution of surface energy decreases. Consequently, the material with larger grains tends to have a more stable structure compared to a material with smaller grains. It is predicted that the substitution of Ru in the main phase results in an increase in the stability of the produced powders. This increased stability could be attributed to the changes in grain size and surface energy discussed earlier. In such a scenario, the crystallinity of the material is expected to improve, leading to more intense peaks in the XRD pattern, as indicated in Table S1 (Supporting Information). This improvement in crystallinity is often associated with increased stability and enhanced material properties. Figure S5a–c (Supporting Information) depicts the EDX-dot mapping analysis of x = 0.1, 0.3, and 0.5 Ru-substituted samples. The analysis reveals that Na, Mn,

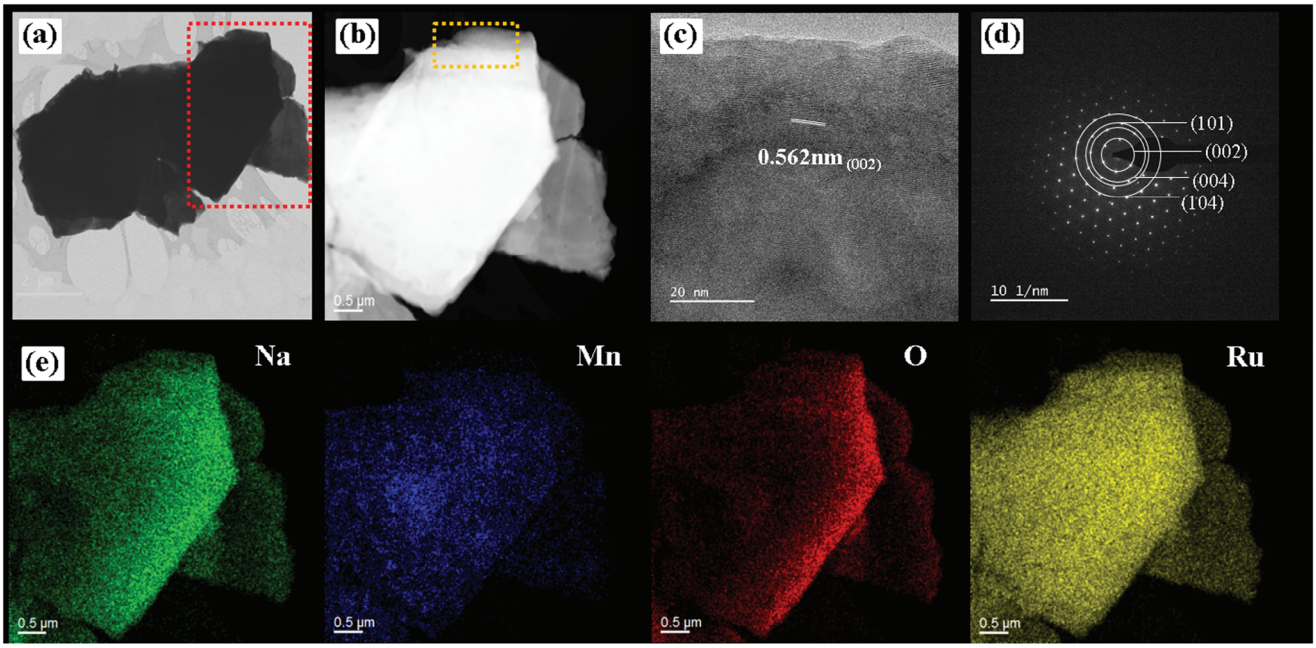


**Figure 2.** High magnification a) TEM and b) STEM images of Ru-doped NMO. c) HR-TEM images and SAED pattern of the selected area in (b). e) EDS element mapping of Na, Mn, Ru, and O for the optimized $Na_{0.67}Mn_{0.6}Ru_{0.4}O_2$ Ru-substituted cathode material.

and Ru ions are uniformly distributed on the surface. Additionally, for the x = 0.5 sample, the Ru ions exhibit a rod-type formation, which corresponds to the $Na_2RuO_3$ phase in the sample. This feature can be easily observed in Figure S5c (Supporting Information). To further probe the structure of the pristine and Ru-substituted cathode materials, HR-TEM and STEM characterizations, displayed in **Figure 2**, were carried out for the sample where x = 0.4. TEM and STEM images of Ru-substituted cathode materials are shown in Figure 2a,b. HR-TEM images (Figure 2c) and SAED pattern (Figure 2d) show that the atomic ordering and hexagonal crystal symmetry after Ru-substitution are similar to that of pristine NMO ($P6_3/mmc$ symmetry), suggesting that the atomic ordering of the structure along the c-axis is well-preserved after Ru-substitution. Figure S6a–d (Supporting Information) exhibits that NMO presents the (002) lattice fringes with a uniform spacing of 5.60 Å. In contrast, the spacing of (002) lattice fringes in Ru-substituted NMO is increased to 5.62 Å, suggesting the expansion of $Na^+$ layer spacing after Ru doping, which is well consistent with the XRD results discussed earlier. Elemental mapping indicates that Na, Mn, Ru, and O elements are homogenously distributed in both pristine NMO and Ru-NMO materials.

To gain more insight into the chemical structure of NMO after Ru-doping, time-of-flight secondary-ion mass spectroscopy (TOF-SIMS) was employed. TOF-SIMS is well suited for characterizing the surface and buried chemical species. The surface layer of pristine and Ru-substituted NMO are directly visualized in **Figure 3**a,b, respectively. The outer layer of pristine NMO reveals that the surface is mostly comprised of Mn–O and oxygenated species. However, for the Ru-substituted NMO, the Na–O has covered more surface area. For further verification, the normalized depth profiles of the chemical species along with their individual spacial distributions in Ru-doped NMO are shown in Figure 3c,d. It could be confirmed from Figure 3d that the outer layer of the surface is comprised of sodium and oxygenated-based species, while the inner layer mainly contains Ru–O and Mn–O. It is worth noting that the Ru-substituted NMO has a high content of $RuO_2$ (i.e., $Ru^{4+}$) as discussed in the XPS study. In contrast, the $MnO_2$ (i.e., $Mn^{4+}$) species have lower content at the outer surface, however, it increases with the increase in depth. Figure 3c demonstrates 3D localization of the representative secondary-ion fragments contained in the Ru-doped NMO, whereby the formation of $Na_2RuO_3$ can be expected corroborating the XPS and XRD results.

To further support physicochemical and electrochemical results of the Ru doping in pristine NMO, density functional theory (DFT) calculations were conducted. The introduction of Ru modifies the density of states (DOS) near the Fermi level, thereby increasing the availability of electronic states in the conduction band and reducing the bandgap across various sodium intercalation levels ($x_{Na}$). The partial density of states (pDOS) for NMO and Ru-NMO at $X_{Na}$ = 0.0, 0.25, 0.5, 0.75, and 1.0 are shown in **Figure 4**a–e. At $X_{Na}$ = 0, the bandgap of NMO is ≈1.6 eV, which narrows down to 1.147 eV upon Ru doping. This reduction in bandgap allows more valence electrons to occupy conduction band orbitals at lower energy levels, consequently enhancing the electronic conductivity.[44] The higher electronic conductivity leads to better rate capability which will be discussed later.

The oxidation states of transition metals in a compound can be inferred from their magnetization value. This is because the magnetic moment of an atom is directly related to its electronic configuration and number of unpaired electrons, which in turn determines its oxidation state. In pristine NMO, Mn atoms primarily exist in the +3 ($t_{2g}^3$ $e_g^1$) and +4 ($t_{2g}^3$ $e_g^0$) oxidation states as shown in **Figure 5**a. The high-spin state $Mn^{3+}$ with its anisotropic electronic structure exhibits Jahn–Teller distortion

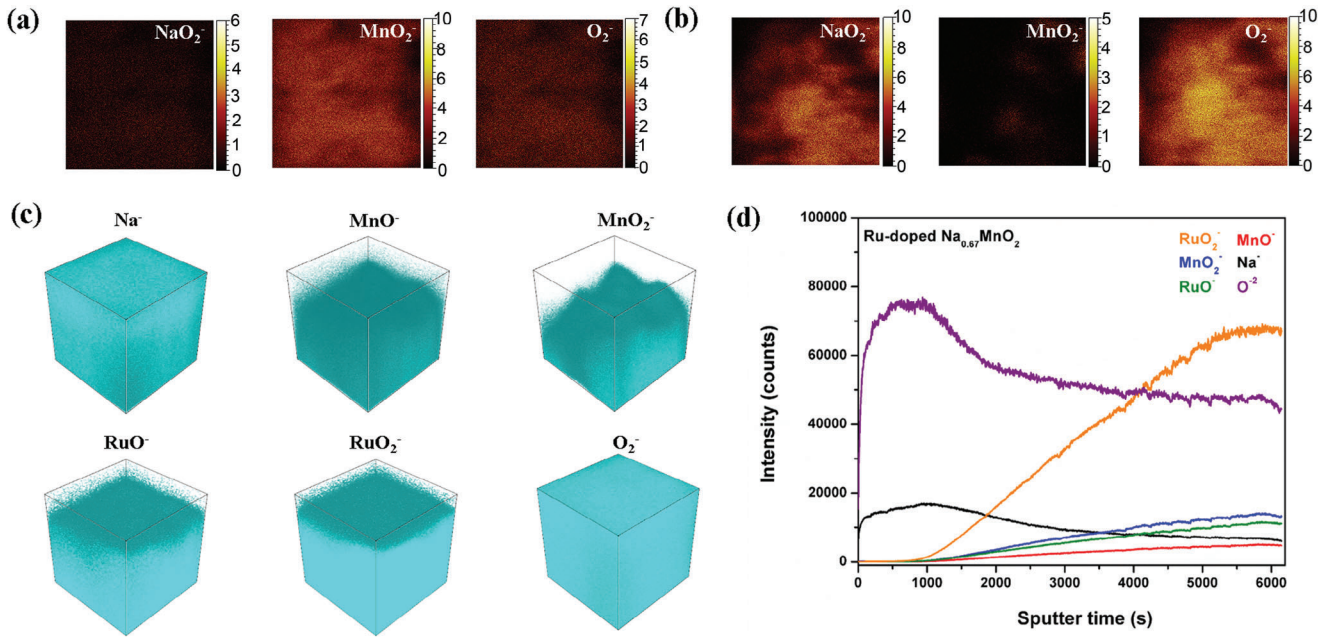


**Figure 3.** TOF-SIMS chemical mapping after the scavenging process, showing the distribution of $NaO^-$, $MnO_2^-$, and $O_2^-$ for a) pristine and b) Ru-substituted of $Na_{0.67}Mn_{1-x}Ru_xO_2$ where x = 0.4. c) Individual spatial distributions and d) TOF-SIMS spectra of $Na^-$, $O^-$, $MnO^-$, $MnO_2^-$, $RuO^-$, and $RuO_2^-$ secondary-ion fragments over 500 s $Cs^+$ sputtering along the depth profile of the Ru-substituted (x = 0.4) $Na_{0.67}MnO_2$ after scavenging processes.

due to one unpaired electron in the $e_g$ orbital. In Ru-NMO ($Na_{0.67}Mn_{1-x}Ru_xO_2$ where x = 0.4), Ru primarily exists in the $4^+$ ($t_{2g}^2\ e_g^0$) and $5^+$ ($t_{2g}^3\ e_g^0$) oxidation states as illustrated in Figure 5b. As the $Ru^{4+}$ and $Ru^{5+}$ have no electron in the $e_g$ orbital, they do not exhibit Jahn–Teller distortion. The higher electronegativity of Ru alters the electronic structure of Mn atoms, causing a redistribution of Mn oxidation states. At $0.75 \leq X_{Na} \leq 1$, some Mn atoms change from $3^+$ ($t_{2g}^3\ e_g^1$) to $2^+$ ($t_{2g}^3\ e_g^2$). This even distribution of unpaired electrons between the $t_{2g}$ and $e_g$ orbitals further reduces Jahn–Teller distortion. Additionally, the wider distribution of magnetization values for oxygen indicates increased participation in redox reactions due to the higher electronegativity of Ru, as shown in Figure 5c. The formation energy curves for both NMO and Ru-NMO are shown in Figure 4f. The reduction in formation energy in Ru-NMO is due to the presence of stronger Ru—O bonds and the stabilizing effect of Ru-doping on $MnO_6$ octahedra, which decreases the Jahn–Teller distortion associated with $Mn^{3+}$.[45] This leads to a more structurally stable crystal structure, thereby improving cycling stability. Overall the benefit of Ru doping on the structure stability is further evidenced by the magnetization calculations.

The bond lengths of transition metal layers significantly influence the properties of layered cathode materials. These bond lengths are effected by the difference in the ionic radii as well as oxidation states of the ions present in the crystal structure. In NMO, the Mn—O bond length increases and attains a wider distribution when Na content increases as shown in Figure 5d. A similar trend can be observed in the Mn—O and Ru—O bonds in Ru-NMO structure as depicted in Figure 5e,f, respectively. This variation can be attributed to the presence of differently charged transition metals in the crystal structure affecting their bonding with oxygen atoms.

### 2.2. Half-Cells Test Results

The electrochemical analysis of the Ru-doped cathode electrodes was performed using a half-cell configuration in CR2032 type coin cells. **Figure 6a** shows the CV graphs of the cells containing different degree of Ru doping. It is well known that the un-doped P2-type $Na_{0.67}MnO_2$ cathode has several peaks during the oxidation process. It is speculated that the peaks below 3.8 V are due to single-phase intercalation or continuous-phase transition. It has been reported that O2-P2 phase transition takes place above high voltage region in the cells.[45] We believe that the number of oxidation peaks in the CV is explained by the alteration of the crystal field around $Na^+$ ions which causes the change of the desodiation energy due to phase transitions in the materials. When P2-type $Na_{0.67}MnO_2$ cathode is substituted, it exhibits only two redox reaction peaks at ≈2.4 and 4.0 V (for example, in $Na_{0.67}Mn_{0.5}Fe_{0.5}O_2$ cathodes). Previous studies suggest that the phase transitions during charging and discharging of a cell can be prevented by doping or substitution.[20,21] When examining the Ru-substituted cathodes, it is evident from the cyclic voltammetry (CV) graphs that two redox peaks appear at 2.25 and 4.04 V.

When we increase the Ru content from 0.05 to 0.2, we observe that the first (≈2.25 V) and second redox peaks (4.04 V) shifted to lower voltage region and there are two new redox peaks (2.05 and 3.82 V) for samples where $0.2 \leq x \leq 0.5$. As previously discussed in the XRD section, there is a $Na_2RuO_3$ impurity phase for a high level of Ru doping in the sample, i.e., x = 0.5. When analyzing the differential capacity (dQ/dV) curve of $Na_2RuO_3$, distinct redox reaction peaks are observed ≈2.6 V, which do not align with the peaks observed in the Ru-substituted P2-type materials.[46] The decrease in the intensity or the emergence of new redox reaction peaks in the cyclic voltammetry (CV) of Ru-substituted materials

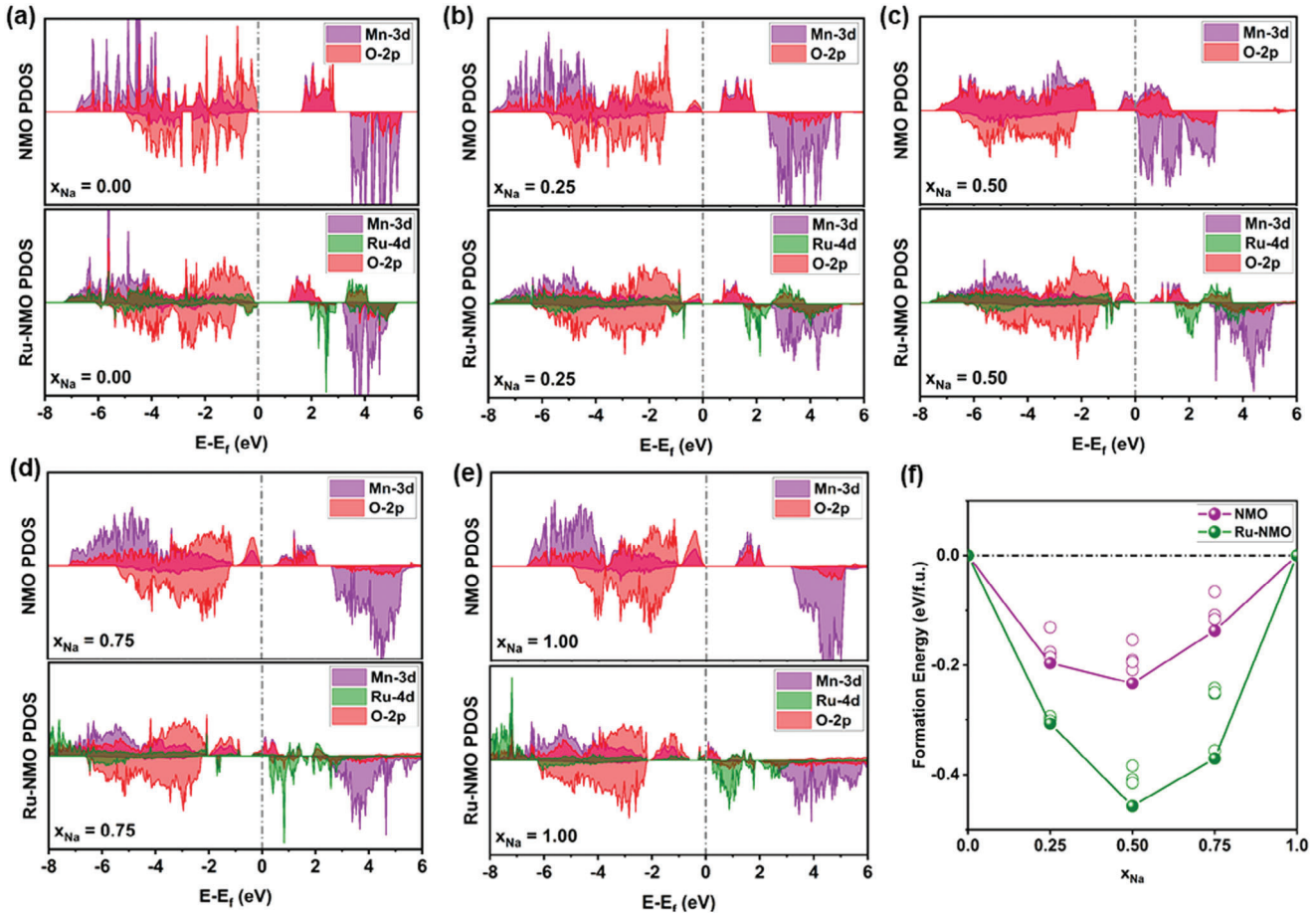


**Figure 4.** a–e) Partial Density of States (pDOS) of Mn 3d, Ru 4d, and O 2p electrons for NMO and Ru-NMO at different Na content $X_{Na}$ = 0, 0.25, 0.5, 0.75, and 1. f) Formation energies of NMO (purple) and Ru-NMO (green) with varying Na content.

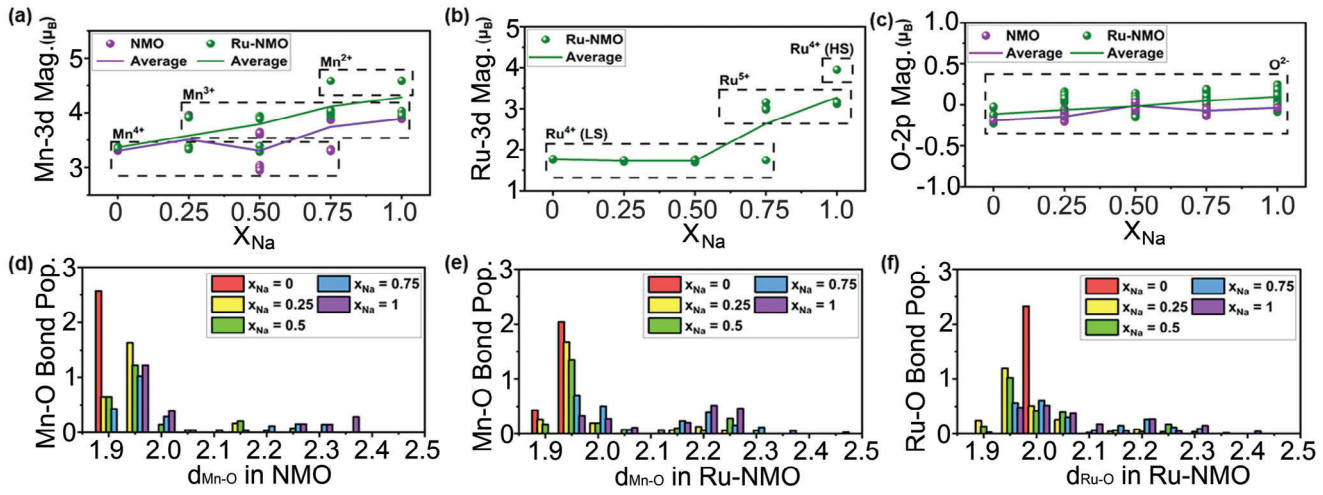


**Figure 5.** a) Magnetization of Mn atom in NMO and Ru-NMO (x = 0.4). b) Magnetization of Ru atom in Ru-NMO. c) Magnetization of O atom in NMO and Ru-NMO. d) Mn—O bond length in NMO at different Na content. e) Mn—O bond length in Ru-NMO at different Na content. f) Ru-O bond length in Ru-NMO at different Na content.

 

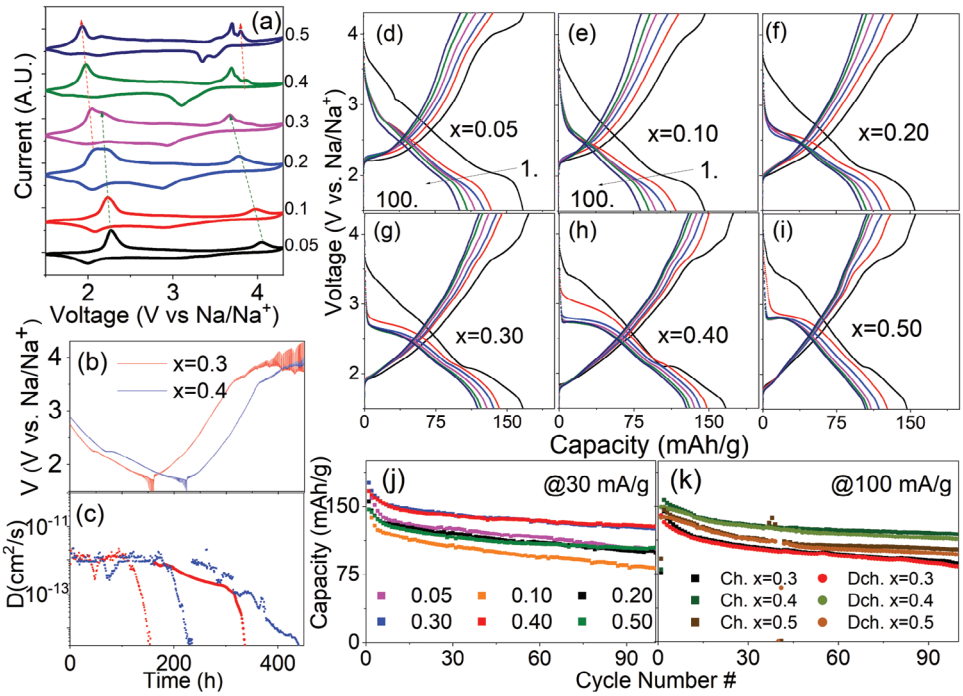


**Figure 6.** a) CV analysis of the half cells for Ru-substituted cathodes, b) GITT experiment for x = 0.3 and 0.4, c) Diffusion rate-time graphs for x = 0.3 and 0.4, Voltage-capacity graphs for d) x = 0.05, e) 0.1, f) 0.2, g) 0.3, h) 0.4, i) 0.5, and capacity cycle number graphs for j) C/3 and k) 1C rates. X varies in $Na_{0.67}Mn_{1-x}Ru_xO_2$ cathode structure.

is caused by alterations in crystal fields. When examining the transition metal (TM) ions within the crystal structure of P2-type materials, the substitution typically involves replacing $Ru^{4+}$ with $Mn^{4+}$ initially to maintain charge balance in the structure. Subsequently, these ions may migrate to $Mn^{3+}$ sites within the lattice. It is known that Ru ions have a higher electronegativity than Mn ions. This difference can lead to an increase in the attractive force for oxygen ions and result in shorter Ru—O bonds compared to Mn—O bonds within the structure. In the second scenario, the $Ru^{4+}$ ions exhibit a greater attraction to oxygen ions compared to $Mn^{3+}$ ions in the structure, primarily due to the electrostatic force between them. For this assumption, the oxygen ions near the $Na^+$ layers will move away from these layers. This movement can lead to a reduction in the redox voltage of the cells. The data for the Na-layer distance in Table S1 (Supporting Information) also aligns with these findings. We hypothesize that there are two distinct structures present in the samples. The shift of the peaks to lower voltage and the appearance of new peaks can be attributed to these structural effects.

The diffusion rate of the Na-ions plays a key role in the battery performance of the cells. There are static and dynamic techniques for the calculation such as Randles–Ševčík equation by measuring scan rate on the peak current ($I_p$)[47] and Galvanostatic Intermittent Titration Technique (GITT),[48] respectively. Figure S7a–f (Supporting Information) shows the CV graphs of all the samples studied herein at the scan rate of 0.1, 0.2, 0.3, 0.4, and 0.5 mV $s^{-1}$. The $I_p$-$v^{1/2}$ graphs were presented in Figure S8a (Supporting Information) and the calculated diffusion coefficient from the slope of the curves was presented in Table S2 (Supporting Information). It is found that the static D value was $4.062 \times 10^{-12}$ $cm^2$ $s^{-1}$ for the sample where x = 0.4 which is the highest value among the others. Similar D values are obtained from the GITT measurement.[49] Figure 6b shows the GITT analysis of the x = 0.3 and 0.4 cells. The details of the GITT analysis were given in our previous paper.[20] The diffusion coefficient can be calculated dynamically at each step by the given equation in reference.[20] The data is plotted in Figure 6c. It should be noted that the point where the discharge transitions to the charging region in the GITT data exhibits a significant jump in the diffusion rate, which is crucial for the analysis. The first diffusion rate for the OCV was obtained as $1.7 \times 10^{-12}$ and $5.8 \times 10^{-12}$ $cm^2$ $s^{-1}$ for x = 0.3 and 0.4, respectively. Afterward, they decreased to $1.5 \times 10^{-15}$ and $3.7 \times 10^{-15}$ $cm^2$ $s^{-1}$ at 1.5 V during the discharge for x = 0.3 and x = 0.4, respectively. After fully discharging, the D values jumped from $0.95 \times 10^{-12}$ to $1.1 \times 10^{-12}$ $cm^2$ $s^{-1}$ during the initial portion of the charging process. It is also fair to conclude that when the state of charge increases, the D values decrease in the cell. When we compare the diffusion coefficient values obtained from the GITT (for the first cycle of GITT data) and CV measurements (as $3.1 \times 10^{-12}$ $cm^2$ $s^{-1}$), we find that the results from both methods are consistent with each other. Another important aspect of the CV data is that different scan rates provide insights into the diffusion mechanism of the electrode materials. The peak current ($i_p$) of the CV data can be explained with the power law in the form of $i_p = av^b$ where $v$ is the scan rate, $a$ and $b$ are the constant parameters. The value of $b$ gives the information for electrochemical reaction mechanisms such as diffusion-controlled ($b = \approx 0.5$) and capacitive reactions ($b = \approx 1$).[50] Figure S8b (Supporting Information) presents the $\log i_p$–$\log v$ graphs and the calculated $b$ values are obtained as 0.45, 0.49,

0.75, 0.74, 0.71 for x = 0.05, 0.1, 0.2, 0.3, 0.4, and 0.5, respectively. Increasing the Ru content leads to an increase in the capacitance contribution to the cells for x values between 0.3 and 0.4, but this contribution decreases as the Ru content increases further. It is because of this effect; we observe higher specific capacities than pure NMO cathodes. This observation is explained further below.

The half-cell capacity-voltage graphs of Ru-substituted cathodes for C/3 were presented in Figure 6d–i and the cycle life analysis of the cells at C/3 were given in Figure 6j. The calculated battery cell performance parameters are given in Table S2 (Supporting Information). In our study, we observed that the highest initial capacity was 176 mAh $g^{-1}$ for x = 0.3, while the highest capacity retention of 77% was recorded for x = 0.4 cells. We should indicate that the theoretical capacity values of the cells were calculated by the equation of $Q = n.F/M$ (as given in Table S2, Supporting Information) where $Q$, $n$, $F$, $M$ are capacity, number of Na ions of a unit formula, faraday constant, and $M$ is the molar mass, respectively. When we calculated the capacity of the cathodes, we can see that the cells for x = 0.3–0.5 show higher capacity values than that of the theoretical expectation. To understand this behavior, we evaluated the CV and chemical formula of the un-doped and doped cells. According to the theoretical calculation, the P2-type $Na_{0.67}MnO_2$ cathode has a capacity of 175 mAh $g^{-1}$ which is higher than that of the Ru-substituted one. When examining the unit cell of the cathode, we observe distinct regions rich in manganese (Mn) and ruthenium (Ru), indicating the presence of two structures with identical lattice symmetry. We can infer that the theoretical capacity expectation of the cells should fall between these two phases present in the samples, which is higher than the calculated values. This idea can be supported by the redox peaks in CV graphs which there are extra peaks for $0.2 \leq x \leq 0.5$ cathodes.

The capacity–voltage graphs of the samples where x = 0.3, 0.4, and 0.5 at 1-C rate were presented in Figure S9a–c (Supporting Information) and the cycle life graphs were displayed in Figure 6k. Furthermore, the battery performance parameters were plotted in Table S2 (Supporting Information). The first capacity values at 100 mA $g^{-1}$ rate were obtained as 140, 149.1, and 137.3 mAh $g^{-1}$ for the samples where x = 0.3, 0.4, and 0.5, respectively. The best capacity retention value, that is as 77% after 100 cycles, was obtained for the cathode where x = 0.4 among the other cells. Though Co is both expensive and toxic, Co substitution can also enhance the cycle life of P-type layered sodium transition metal oxide cathode material. Zhang et. al. synthesized P2/P3–$Na_{0.67}Mn_{0.64}Co_{0.30}Al_{0.06}O_2$ cathode active material via dealloying–annealing method. The cell delivered specific capacity of ≈80 mAh $g^{-1}$ after 500 cycles.[51] Li et. al. synthesized Li and Ti doping in to Layered manganese-based oxides producing hexagonal P2-$Na_{0.643}Li_{0.078}Mn_{0.827}Ti_{0.095}O_2$ structure. Their cell also revealed a capacity of 90 mAh $g^{-1}$ after 500 cycles though it was a half-cell result.[52] Xu et. al. produced P2-type $Na_{0.67}Mn_{0.6}Fe_{0.4}O_2$ cathodes with a capacity of ≈200 mAh $g^{-1}$ with a capacity fade value of 23.7% at 0.1C-rate after 100 cycles.[53] Marino et. al. produced $Na_{0.67}Mn_{0.6}Fe_{0.25}Co_{0.15}O_2$ phase and they found that the capacity of the cells reached 142 mAh $g^{-1}$ at C/10 rate after 100 cycles.[54] Existing studies suggest that substituting Fe in P2-type $Na_{0.67}MnO_2$ has a more favorable impact compared to other transition metals. Since Fe and Ru are in the same column of the periodic table, they may have similar effects despite their different masses. During de-sodiation, the transition metal oxide structure is expected to maintain its symmetry. The mass of ions plays a crucial role in the vibration modes of a crystal structure, affecting factors like amplitude and frequency. Substituting lighter elements with heavier ones can reduce the thermal vibration, potentially improving the stability of the de-sodiated structure's skeleton, as mentioned in the reference.[55] Therefore, we judiciously selected Ru to be an ideal candidate for swapping Mn to enhance the cell performance. The C-rate measurements of the cells were presented in Figure S10 (Supporting Information) and the highest capacity for C/10-rate was obtained as 155.7 and 164.2 mAh $g^{-1}$ for x = 0.3 and 0.4, respectively. The capacity of the cells at 3C rate was found as 85.6 and 104.9 mAh $g^{-1}$ for x = 0.3 and 0.4, respectively. It is therefore concluded that the Ru-substituted P2-type $Na_{0.67}MnO_2$ has good performance at the high rate applications.

The EIS analysis of the samples is given in Figure S11 (Supporting Information) with the EQC model presented in the inset of Figure S11 (Supporting Information). There are three different parts in the EQC model; the first is the $R_B$ which is the equivalent to resistance for the electrolyte, current collectors, and electrode materials, the second region in the EQC which has the first parallel branch ($Q_1$-$R_1$) can be explained by the SEI layer in the cells and the last part can be explained by the charge-transfer resistance, double layer capacitance and Warburg parameter which are related to diffusion of the Na-ions in the electrode.[56] The fitting parameters are presented in Table S3 (Supporting Information). It is seen that the $R_B$ values increased by Ru doping and revealed a plateau for the samples where $0.2 \leq x \leq 0.4$ at ≈5–6 Ohm. Although the $R_B$ value is almost the same for the different SOC values, it can increase by the depletion of the electrolyte and micro crack formation in the particles during the cycling process. It is well known that the first semicircle in EIS measurements can be explained by the impedance of a layer between the electrode and electrolyte which is the second part of the EQC model. We should note that the $R_{SEI}$ is very sensitive to the content of the electrolyte in the cells.[57] The obtained $R_{SEI}$ values in the cells are very close to each other which is the expected since the electrolytes in the cells have the same contents. In the last part of the EQC, $R_{ct}$ is related to the kinetics of an electrochemical reaction which is affected by the surface coating, phase transition, bandgap structure, and particle size.[56,57] We observed that the $R_{ct}$ values in Table S3 (Supporting Information) have the same range which can be explained by similar properties of the electrodes in the cells. Looking at the EIS elements in Table S3 (Supporting Information), we find that the highest W value is associated with the x = 0.4 Ru-substituted sample. This value is indicative of the diffusion rate of Na-ions within the system.

### 2.3. Operando Structural Analysis

**Figure** 7a shows the in situ XRD data of the cathode, $Na_{0.67}Mn_{1-x}Ru_xO_2$ where x = 0.4, containing cells during the first two cycles. The strong peaks observed in the XRD data are due to the Al current collector. We focused on the (002), (004), (100), and (114) peak shifts during the cycling. During the charging process, the solid solution mechanism is revealed by the noticeable shift of the (004) peak toward lower angles and the (100) peak toward

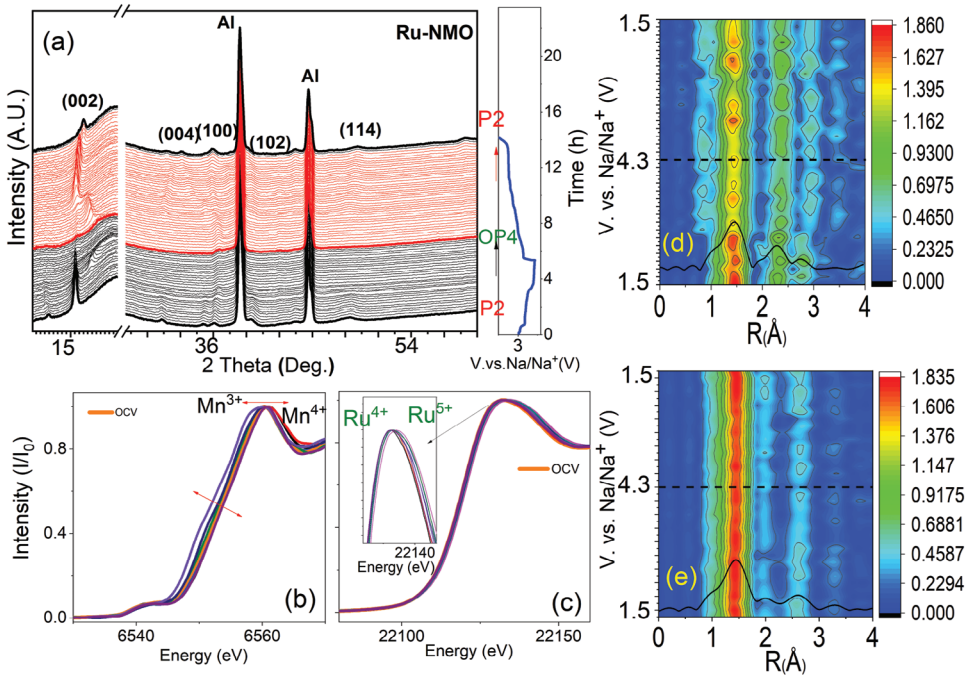


**Figure 7.** a) Structure evaluation of $Na_{0.67}Mn_{0.6}Ru_{0.4}O_2$ Ru substituted cathode during charge and discharge process with right panel showing phase transition from P2-OP4-Cmcm upon sodium extraction and re-insertion into the structure. The XAS spectrum of b) Mn K-edge and c) Ru K-edge depends on the charging and discharging process. The counter plot of FT of EXAFS for d) Mn and e) Ru K-edge during charge and discharge process of $Na_{0.67}Mn_{1-x}Ru_xO_2$ where x = 0.4. The mapping data was calculated using OCV FT of XAS for Mn and Ru K-edge and it was subtracted from the FT of XAS graphs for different voltages.

higher angles which the counter plot of this trend presented in Figure S12 (Supporting Information). This trend corresponds to an expansion along the 'c' axis and a reduction along the 'a' axis. These lattice alterations occur during the removal of the sodium ions. As a result, a repulsive effect between the metal-oxide layers takes place instigating the expansion in the 'c' direction.[58] At this stage, the active material displays a dual-phase region consisting of the P2 and OP4 phases. Upon further increasing the voltage to 4.3 V, the structure completely transitions to the OP4 phase. We should indicate that the phase transitions between the P2 and OP4 phases during the charge and discharge process have a reversible property as obtained in the previous studies.[59,60] It was observed that the intensity of the reflection planes in the XRD pattern is related to the OP4 phase. This phenomenon diminishes as the sodium content increases throughout the discharge process, eventually disappearing at ≈3.0 V.[61] At the last stage of the discharge (down to 1.5 V), the cell exhibits a more complex behavior, revealing a dual-phase region comprising the P2 and P2' (Cmcm) phases.[62] When Na content is more than ≈0.8 per formula unit, the number of $Mn^{3+}$ ions increases triggering Jahn–Teller distortion that leads to a partial phase transition from P2 to P2'.

It is stated that the c-lattice parameters during the charging process (during Na+ extraction) increase and it is expected that the peak shift of (002) and (004) reflection planes to lower angles due to the repulsive electrostatic force between the neighboring oxygen layers. Peaks on a-b planes such as (112) or (114) reflection lines shift to higher angles because of the smaller ion radii of Mn at the valence state of 4+[63] which we also observed. Notice that the OP4 phase begins to appear after extracting 0.39 mol $Na^+$ and persists until full charge, indicated by the characteristic OP4 (004) peak at 17.5° in the structure.[64]

The in situ XAS studies were performed using a modified version of CR2032 coin cell where the cell allows X-ray penetration via the Kapton window.[20] The XANES data was collected for the K edge of Mn and Ru elements for the x = 0.4 Ru substitution cathode active material during cycling. The XANES spectrums were presented in Figure 7b,c. It is evident that both Mn and Ru elements shifted toward higher energies during charging, indicating the oxidation of the Mn and Ru transition metals. This further advocates that these two elements contributed to the charge capacities. A clear peak position difference in the spectra of the Mn K-edge was observed between the XANES at OCV (6559.4 eV) and the 4.3 V charged (6560.9 eV) electrodes in the cells. According to the reference data of $Mn^{3+}$($Mn_2O_3$) and $Mn^{4+}$($MnO_2$), the XANES peaks (Figure S13, Supporting Information) were observed at 6558.8 and 6561.2 eV (showing an increase of 2.4 eV in energy) for $Mn^{3+}$ and $Mn^{4+}$, respectively. Therefore, it is clear that the $Mn^{3+}$ ions transform to $Mn^{4+}$ions, albeit slightly lower oxidation state, during the charging process. The process is reversible as shown with the energy values in the XANES figure. The orange color in both Figure 7b,c indicates that the data were recorded during rest, i.e., OCV. During charging the peak is gradually shifting higher energies and during the discharge the peak is shifting even below the OCV line as shown with purple color. The XANES peaks of Ru K-edge were given in Figure 7c and it is seen that the peaks for OCV and 4.3 V were observed at 22 132.8 and 22 134.4 eV, (showing an increase of 1.6 eV in energy), respectively. The reference XANES data of Ru metal, $Ru^{3+}$ ($RuCl^3$), and $Ru^{4+}$ ($RuO_2$) were presented in literature.[65] The XANES

data for OCV corresponds to $Ru^{4+}$ and the spectra of Ru K-edge gradually shifted to higher energies due to the oxidation of Ru ions from 4+ to 5+ as indicated in the literature.[65] It was previously calculated that the energy shifts values for $SuRuO_3$ and $Sr_2GdRuO_6$ were found as 1.5 eV stemming from the oxidation of Ru from 4+ to 5+.[66] Similar energy change was also found for our samples indicating oxidation state change from 4+ to 5+. Similar phenomena with respect to energy changes during charge and discharge were also seen in Ru however this change was much smaller than that of Mn. Because of this, we could not see the shift of the Ru peak back and forth as clearly as Mn one. To analyze the local structure around Mn and Ru ions in the x = 0.4 Ru-substituted containing half-cell, the Fourier Transform (FT) EXAFS maps from XAS data during galvanostatic measurements were generated using the Athena program. The results are displayed in Figure 7d,e as contour plots. The first and the second peaks in the corresponding EXAFS data reveals the metal-oxygen and metal–metal bonds, respectively. The bond lengths were calculated using the Artemis program. The fitting results at different cycles of the battery are plotted in Figure S14 (Supporting Information). The fitting parameters were optimized for each case in detail as reported in the literature.[67] The P63/mmc symmetry was employed for the calculations, and the fitting of Mn and Ru was performed using the first scattering path of the data. The best-fit values of the structural parameters for OCV and 4.3 charged state are listed in Table S4 (Supporting Information). The symbol $N$ represents the number of neighboring atoms, while the $S_0^2$ denotes the amplitude reduction factor, typically found within the range of $0.7 < S_0^2 < 1.0$.[64] Additionally, the $R$ (Å) is the radial distance to the neighboring atom, the $\sigma^2 (Å^2)$ is the mean-square disorder in $R$. The latter notion was named as Debye-Waller factor which is related to the correlation of atomic motion in the structure and can give information on the vibrational dynamics of the structure. This critical information can reveal the displacements of atoms from their idealized positions.[67] The symbol $\Delta E$ represents the energy difference between creating a photoelectron with energy $(E - E_0)$ where $E$ is the energy of the incident X-ray that causes an atom to absorb, and $E_0$ is the energy of the core electron that is destroyed. It should be noted that there could be different bond lengths for TM-O and TM-TM in the structure. According to Mn EXAFS data, the bond lengths of Mn-O, Mn–Mn, and Mn–Ru were calculated as 1.94, 2.89, and 3.20 Å, respectively. This is expected because the repulsive force of Mn-Mn is lower than that of Mn–Ru in the structure. It was found in the literature that the Mn–O and Mn–Mn bond lengths for P2-type $NaMnO_2$ were calculated as 1.907 and 2.898 Å, respectively which are close to the parameters we fitted at OCV.[68] For the similar substituted elements in the form of P2-$NaMn_{0.9}Fe_{0.1}O_2$, it was found that the bond lengths were increased from 1.908 Å (Mn–O) and 2.901 Å (Mn–Mn) to 1.998 Å (Mn–O) and 2.905 (Mn–TM) by Fe doping.[65] Since Fe and Ru are in the same column of the periodic table, we expected a similar outcome when doped into the same cathode. When the Na-ions are left from the lattice during the charging process, it is expected that Mn—O bonds decrease since the Na–O interaction is almost canceled in the structure. As for the bond lengths of the Mn–TM ions, it was observed that a stable structure existed for the bond structure, yielding improved stability of the lattice structure. Yabuuchi et. al. investigated the bond length of Fe–O in P2-type $Na_xFe_{0.5}Mn_{0.5}O_2$ cathode and they found that the bond length of Fe–O at pristine state was changed from 2 to 1.90 Å when charged to 4.2 V.[64] In contrast, the Ru—O bond length was not affected during the charging and discharging process providing a more stable structure.

### 2.4. Full-Cell Test Results

The full cells are assembled by using x = 0.3 and 0.4 Ru-substituted cathodes against commercial hard carbon anodes. We used a pre-sodiation technique for the anodes in which the details can be found in our previous papers.[20,69] The cyclic voltammetry (CV) of the x = 0.3 and x = 0.4 Ru-substituted full cells is presented in **Figure 8**a. It is observed that there are four different redox peaks during the charging process, which were discussed in the half-cell section, previously. The redox peaks observed in the full cell also corroborate the data from the half-cell experiments. Figure 8b,c shows the voltage-capacity graphs of the cathode where x = 0.3 against hard carbon and the cathode where x = 0.4 against hard carbon full cells at different discharge rates. We utilized the following recipe for the cycle life assessment of the full cells as seen in Figure 8d: C/10 rate for 1 cycle, C/3 rate for 1 cycle, C/2 rate for 1 cycle, and 1C rate for 500 cycles. The obtained capacity values were presented in Table S2 (Supporting Information) and it is found that the first capacity for x = 0.3 and 0.4 full cells were obtained as 116 and 136 mAh $g^{-1}$ and they were decreased to 66 and 86 mAh $g^{-1}$ after 500 cycles, respectively.

The capacity retention values for 500 cycles were obtained as 57% and 67% for x = 0.3 and x = 0.4 full cells, respectively. Obtaining close to 70% capacity retention after 500 cycles at 100% DOD in a sodium ion full cell is outstanding. It is evident from Figure 8e that the cells containing cathode where x = 0.4 exhibits better performance at 1C rate. However, high current rates can lead to increased capacity loss for the cells containing cathode where x = 0.4. We also evaluated the rate dependency of the cells containing cathode where x = 0.3 and x = 0.4. The cell containing the cathode where x = 0.4 exhibited better full-cell performance compared to the cell containing the cathode where x = 0.3. Although there is an impurity phase of $Na_2RuO_3$ for x≥0.4, it should be noted that the capacitive contribution for x = 0.4 is higher than that of x = 0.3, which could enhance the battery performance of the cells. The EIS analysis of the full cells is given in Figure S15 (Supporting Information) and the fitting model is presented in the inset of the Figure. In this study, the EIS, as illustrated in Figure S15 (Supporting Information), revealing four distinctive regions diverging from the EIS profile of the half-cell. The initial region (I) exhibiting lower impedance corresponds to the ohmic component, while the subsequent small semicircle (region II) arises from the surface film resistance. Regions III and IV are associated with the cathode and anode, respectively, and the final linear segment at lower frequencies indicates mass transfer phenomena within the cells.[60] The corresponding fitting parameters are tabulated in Table S3 (Supporting Information). Notably, the stark contrast between the full-cell and half-cell EIS profiles is attributed to differences in cell configuration. Interactions between the anode (hard carbon) and Ru-doped cathode give rise to the processes like side reactions, shuttle effects, or alterations in electrolyte composition, thereby affecting the impedance profile. Moreover, in the full-cell setup, the kinetics of both anodic and

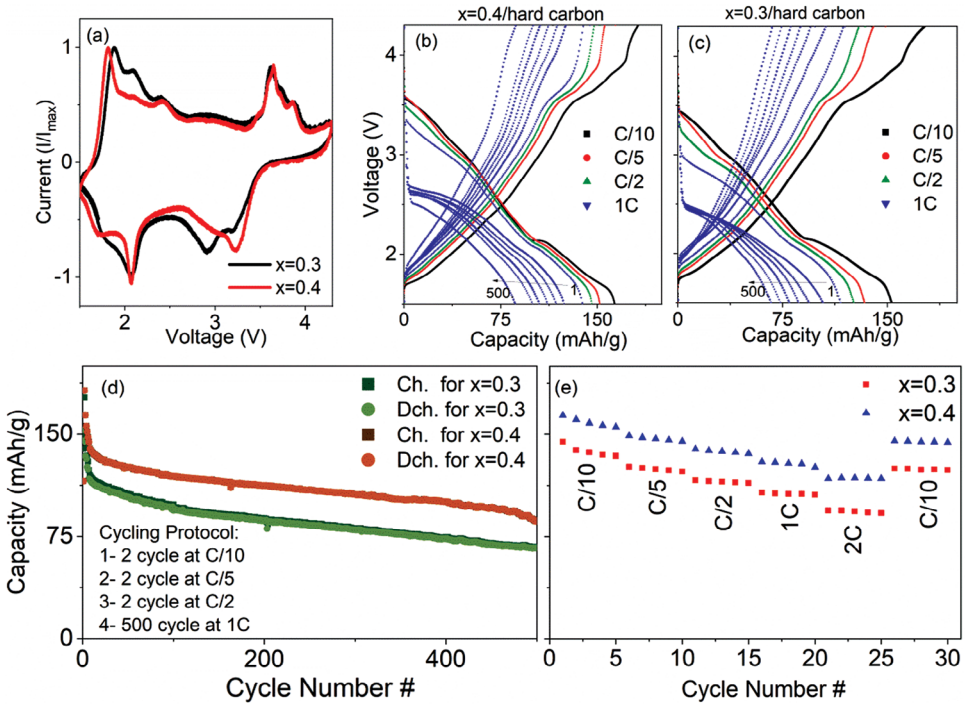


**Figure 8.** a) CV graphs, Voltage–capacity of $Na_{0.67}Mn_{1-x}Ru_xO_2$ where b) x = 0.4 and c) x = 0.3, d) capacity-cycle number graphs up to 500 cycles and e) C-rate data of the full-cells for x = 0.3 and x = 0.4.

cathodic reactions can influence the overall impedance response. This can result in different profiles compared to the half-cell configuration, where typically kinetics of only one of the electrodes are a contributing factor. Moreover, differences in the geometry of the full-cell and half-cell setups, including electrode dimensions, shape, and inter-electrode spacing, can affect the distribution of current and potential gradients within the cell. These geometric differences can change the impedance response by modulating the distribution of electrochemical processes and charge transfer kinetics.[61,44] The initial region ($R_s$ in EQC) exhibiting lower impedance corresponds to the ohmic component, while the subsequent small semicircle ($R_1$ and $Q_1$ in EQC) arises from surface film resistance. The impedance associated with the cathode and anode corresponds to $R_2/Q_2$ and $R_3/O_3$ in EQC, respectively, and the final linear segment at lower frequencies indicates mass transfer phenomena within the cells. The corresponding fitting parameters are detailed in Table S3 (Supporting Information).

## 3. Conclusion

We have investigated the role of Ru in enhancing the cycling capability of the $Na_{0.67}Mn_{0.5-x}RuO_2$ cathode active material. The detailed XRD analysis along with the fitting results confirm that when Ru doping is below x = 0.5, the Ru doping does not reveal any structural impurities. A change in the lattice volume as a function of increasing Ru content is attributed to the different ionic radii for different coordination and valance states of the ions which was supported by the FTIR and Raman spectroscopy measurements. Through in situ X-ray absorption spectroscopy (XAS) and X-ray diffraction (XRD) studies, we have unraveled the role of Ru in the lattice structure. Magnetization calculations revealed the presence of stronger Ru—O bonds and the stabilizing effect of Ru-doping on $MnO_6$ octahedra within the structure. Density of States (DOS) calculations showed that the bandgap of NMO reduced by Ru doping leading to the enhancement of the electronic conductivity of the pure NMO cathode. The performance of the full cell containing $Na_{0.67}Mn_{0.6}Ru_{0.4}O_2$/ Hard Carbon delivered an outstanding battery performance where 67% capacity retention was obtained after 500 cycles at 100% DOD.

## 4. Experimental Section

$Na_2O_2$, $RuO_2$, and $MnO_2$ were used as the starting materials to synthesize $Na_{0.67}Mn_{1-x}Ru_xO_2$ where x varied between 0.05 and 0.5. The initial precursors were mixed using an agate mortar for ≈2 h and pressed to form the pellet under 5 tons of pressure. The Ru-substituted pellets were annealed at 900 °C for 5 h in an ambient atmosphere and quenched using L-$N_2$. After the annealing, the samples were kept in a glove box where oxygen and moisture levels were under 5 ppm. X-ray diffraction analysis was performed using a Malvern Panalytical EMPYREAN (3rd generation) diffractometer, employing a CuK$_\alpha$ ($\lambda_{K\alpha}$ = 1.5405 Å). GSAS-II software was used to analyze the structural parameters.[70] Fourier transform infrared (FTIR) data was collected using a Perkin Elmer Spectrum One spectrophotometer. The spectrophotometer was equipped with NRS-4500 Confocal Raman Microscope with a 532 nm laser located at AYBU-MERLAB, Ankara, Türkiye. Surface morphology and elemental mapping were analyzed using a Thermo Fisher Scientific Apreo Scanning Electron Microscope (SEM) combined with an energy-dispersive X-ray (EDS) unit (Thermo Scientific Ultra Dry Detector). Thermo Scientific K-Alpha system with a monochromatic Al-K$\alpha$ source was used for the XPS analysis located at EMUM-Izmir-Turkey (Detail can be found in ref. [71]

The CR2032 cells were fabricated using the blend of the active material, Super-P carbon, and polyvinylidene fluoride (PVDF) (with a weight ratio of 70:15:15) and were suspended with the proper amount of *N*-Metyl-2-Pyrrolidone (NMP). The mixture was coated on Al foil using a doctor

blade, and later kept in a vacuum furnace at 110 °C for 24 h for drying. The electrodes were punched with 15 mm diameter discs. Na-foil and 1 M $NaClO_4$ (PC/EC = 50/50, w/w) were used as anode and electrolyte, respectively, to assemble CR2032 half-cells. Cyclic voltammetry measurements were conducted between 1.5 and 4.3 V with a scan rate of 0.1 mV $s^{-1}$. Neware BTS4000 and Hefa-cycle BA100A battery analyzers were utilized for charging and discharging the cells. The electrochemical impedance spectroscopy (EIS) test was run from 0.1 mHz to 200 kHz using 10 mV AC amplitude voltage. A full cell containing Ru-doped cathode against a hard carbon anode was also assembled. The details of fabrication and electrochemical characterizations of the full cells are documented in the previous study.[69] To enhance the capacity of the cells, a pre-sodiation strategy was employed, and the galvanostatic discharge–charge–discharge method was used for the pre-sodiation process. Ru-substituted cathode and pre-sodiated hard carbon (provided by Gelon Limited) were assembled in CR2032 coin cells.

X-ray absorption near-edge (XANES) and extended x-ray absorption fine structure (EXAFS) analysis were performed at XAS/XRF Beamline at SESAME located in Allen, Jordan. The fluorescence mode of the beamline was used to collect the XANES/EXAFS data at the Mn, and Ru K-edges at room temperature. Mn and Ru foils were used for calibration and alignment purposes before the data collection. After the calibration and alignment, XAS measurements were recorded during cycling between a voltage window of 1.5–4.3 V at a 30 mA $g^{-1}$ rate. Details of the cell design in this study can be found in the previous study.[20] Analysis of the XAS data was performed by the Athena and Artemis program.[72]

A time-resolved X-ray Diffraction (TR-XRD) instrument was used for in situ XRD measurements at the Korea Institute of Science and Technology located in South Korea. The initial and final angles of the XRD were set to 10°–90°, and the data were collected at 180 s intervals for each scan during the measurement. For the TOF-SIMS studies, an ION-TOF (Münster) was used, where the pressure of the analysis chamber was maintained below $2 \times 10^{-9}$ mbar to produce an ultrahigh vacuum. All the detected secondary ions of interest possessed negative polarity. A pulsed 30 keV $Bi^{3+}$-ion beam was applied for the spectrum and depth profiling. For sputtering the cathode material, a 3 keV $Cs^{+}$-ion beam was used with a typical sputtered area of 200 × 200 µm. Atomic-scale high-angle annular dark field transmission electron microscope (HAADF-TEM) images, along with STEM and HR-TEM images and SAED patterns were investigated by using an FEI Titan TM 80–300 microscope at 300 kV.

Density functional theory (DFT) calculations were conducted using the Vienna Ab initio Simulation Package (VASP) using projector augmented wave (PAW) method.[73–76] Spin-polarized generalized gradient approximation (GGA) was employed with Perdew–Burke–Ernzerhof (PBE) exchange-correlation functional with DFT+U correction.[77,78] To account for the Coulomb interaction between *d*-orbital electrons of transition metals, Hubbard U parameters of 4.95 and 5 eV for Mn and Ru atoms were applied, respectively.[79] The electron configurations of Na ($2p^6 3s^1$), Mn ($3p^6 4s^2 3d^{10}$), Ru ($4p^6 5s^2 4d^{10}$) and O ($2s^2 2p^4$) were treated as the valence electrons. A conjugate gradient algorithm was used for ionic relaxation with a plane wave cutoff energy of 520 eV. For the electronic relaxation, Gaussian smearing with a width of 0.05 eV was used. The convergence criteria for electronic and ionic relaxations were set to 10–5 eV and 0.03 eV $Å^{-1}$ respectively. The Brillouin zone was sampled using an automatic k-point mesh with a Gamma-centered grid of 2 × 4 × 2. The initial structures of both $Na_{0.675}MnO_2$ (NMO) and $Na_{0.675}Mn_{0.6}Ru_{0.4}O_2$ (Ru-NMO) are derived from Rietveld refinements of X-ray diffraction (XRD) data. The supercell program is used to create supercells of 4 × 2 × 1 with varying Na content over a full range of $0 \leq Na_x \leq 1$ and to address the partial occupancy of Mn/Ru in the crystal structure of Ru-NMO.[80] The electrostatic energies of the generated supercell are calculated using the Ewald summation method, as implemented in pymatgen library.[81,82] The generated supercells of NMO and Ru-NMO are shown in Figure S1 (Supporting Information). The formation energy was calculated using the below equation where *E* refers to the total energy of the system.

$$\Delta H = E_{Na_xMn_{1-y}Ru_yO_2} - (1-x)\,E_{Mn_{1-y}Ru_yO_2} - xE_{NaMn_{1-y}Ru_yO_2} \quad (1)$$

## Supporting Information

Supporting Information is available from the Wiley Online Library or from the author.

## Acknowledgements

The authors would like to acknowledge the financial support of Inonu University under project number FBA-2023-3099. The Operando XAS analysis was performed at XAS/XRF Beamline in SESAME-Jordan and TENMAK financially supported the author during to experiment in SESAME. This publication was made possible by the grant of 2232-International Fellowship for Outstanding Researchers Program (project no. 118C307). MNA was also supported by TÜBİTAK-2232 program.

## Conflict of Interest

The authors declare no conflict of interest.

## Data Availability Statement

The data that support the findings of this study are available from the corresponding author upon reasonable request.

## Keywords

Na-ion batteries, PT-type $NaMnO_2$, Ru doped cathode

Received: July 25, 2024
Revised: September 16, 2024
Published online: October 2, 2024

[1] X. Pu, K. Yang, Z. Pan, C. Song, Y. Lai, R. Li, Z.-L. Xu, Z. Chen, Y. Cao, *Carbon Energy.* **2024**, *6*, e449.
[2] J. Wu, M. Zheng, T. Liu, Y. Wang, J. Nai, Y. Liu, L. Zhang, S. Zhang, X. Tao, *Energy Storage Mater.* **2023**, *54*, 120.
[3] Y. Fan, X. Chen, D. Legut, Q. Zhang, *Energy Storage Mater.* **2019**, *16*, 169.
[4] K. Mizushima, P. C. Jones, P. J. Wiseman, J. B. Goodenough, *Mater. Res. Bull.* **1980**, *15*, 783.
[5] Y. Li, M. Chen, B. Liu, Y. Zhang, X. Liang, X. Xia, *Adv. Energy Mater.* **2020**, *10*, 2000927.
[6] Y. Zhang, X. Xia, B. Liu, S. Deng, D. Xie, Q. Liu, J. Wu, Y. Wang, X. Wang, J. Tu, *Adv. Energy Mater.* **2019**, *9*, 1803342.
[7] Y. R. Pei, H. Y. Zhou, M. Zhao, J. C. Li, X. Ge, W. Zhang, C. C. Yang, Q. Jiang, *Carbon Energy.* **2024**, *6*, e374.
[8] M. Mamoor, Y. Li, L. Wang, Z. Jing, B. Wang, G. Qu, L. Kong, Y. Li, Z. Guo, L. Xu, *Green Energy and Resources.* **2023**, *1*, 100033.
[9] S. Zhang, B. Steubing, H. K. Potter, P. Hansson, Å. Nordberg, *Conservation and Recycling.* **2024**, *202*, 107362.
[10] E. Zuo, A. Innocenti, M. Zarrabeitia, D. Bresser, Y. Yang, S. Passerini, *Acc. Chem. Res.* **2023**, *56*, 284.
[11] A. Kanwade, S. Gupta, A. Kankane, A. Srivastava, S. C. Yadav, P. M. Shirage, *Chem. Soc. Rev.* **2021**, *50*, 13189.
[12] Y. Niu, Y. Zhangd, M. Xu, *J. Mater. Chem. A.* **2019**, *7*, 15006.
[13] S. T. Dacek, W. D. Richards, D. A. Kitchaev, G. Ceder, *Chem. Mater.* **2016**, *28*, 5450.
[14] A. Sivakumaran, A. J. Samson, V. Thangadurai, *Energy Technol.* **2023**, *11*, 2201323.
[15] L. Lander, J. Tarascon, A. Yamada, *Chem. Rec.* **2018**, *18*, 1394.

[16] H. Liu, W. Deng, X. Gao, J. Chen, S. Yin, L. Yang, G. Zou, H. Hou, X. Ji, *Nano Select.* **2020**, *1*, 200.
[17] R. Alcántara, C. Vicente, P. Lavela, J. L. Tirado, A. Medina, R. Stoyanova, *Materials.* **2023**, *16*, 6970.
[18] P. Zhang, G. Zhang, Y. Liu, Y. Fan, X. Shi, Y. Dai, S. Gong, J. Hou, J. Ma, Y. Huang, R. Zhang, *J. Colloid Interface Sci.* **2024**, *654*, 1405.
[19] E. Gonzalo, M. Zarrabeitia, N. E. Drewett, J. M. López del Amo, T. Rojo, *Energy Storage Mater.* **2021**, *34*, 682.
[20] E. Dogan, S. Altundag, E. Altin, E. Oz, S. Altin, *Electrochim. Acta.* **2024**, *473*, 143470.
[21] B. Kalyoncuoglu, M. Ozgul, S. Altundag, M. Harfouche, E. Oz, S. Avci, X. Ji, S. Altin, M. N. Ates, *J. Power Sources.* **2024**, *591*, 233775.
[22] J. Hafeez, M. Bilal, N. Rasool, U. Hafeez, S. A. A. Shah, S. Imran, Z. A. Zakaria, *Arabian J. Chem.* **2022**, *15*, 104165.
[23] S. Altin, A. Bayri, E. Altin, E. Oz, S. Yasar, S. Altundağ, M. Harfouche, S. Avci, *Energy Technol.* **2021**, *9*, 2001130.
[24] K. M. Mogare, K. Friese, W. Klein, M. Jansen, *Z. Anorg. Allg. Chem.* **2004**, *630*, 547.
[25] R. D. Shannon, *Acta Cryst.* **1976**, *32*, 751.
[26] A. Maurya, A. Dwivedi, A. Bahadur, *J. Alloys Compd.* **2019**, *786*, 457.
[27] P. W. Menezes, A. Indra, D. Gonzalez-Flores, N. R. Sahraie, I. Zaharieva, M. Schwarze, P. Strasser, H. Dau, M. Driess, *ACS Catal.* **2015**, *5*, 2017.
[28] T. Yamashita, P. Hayes, *Appl. Surf. Sci.* **2008**, *254*, 2441.
[29] A. Khorshidi, N. Sadeghi, *J. Clust. Sci.* **2016**, *27*, 1923.
[30] M. Skunik-Nuckowska, P. Bacal, P. J. Kulesza, *J. Solid State Electrochem.* **2015**, *19*, 2753.
[31] S. Yuri Ponosov, V. E. Komleva, V. S. Streltsov, Raman spectroscopy and density functional theory studies, **2019**, *100*, 134310.
[32] M. Xie, R. Luo, J. Lu, R. Chen, F. Wu, X. Wang, C. Zhan, H. Wu, H. M. Albishri, A. S. Al-Bogami, *ACS Appl. Mater. Interfaces.* **2014**, *6*, 17176.
[33] T. Song, L. Chen, D. Gastol, B. Dong, J. F. Marco, F. Berry, P. Slater, D. Reed, E. Kendrick, *Chem. Mater.* **2022**, *34*, 4153.
[34] P. F. Wang, Y. You, Y. X. Yin, Y. S. Wang, L. J. Wan, L. Gu, Y. G. Guo, *Angew. Chem., Int. Ed.* **2016**, *55*, 7445.
[35] N. Taskiran, S. Altundag, V. Koleva, E. Altin, M. Arshad, S. Avci, M. N. Ates, S. Altin, R. Stoyanova, *Batteries.* **2023**, *9*, 497.
[36] A. P. Savintsev, Y. O. Gavasheli, Z. Kh Kalazhokov, K. K Kalazhokov, *J. Phys.: Conf. Series.* **2016**, *774*, 012118.
[37] W. Zuo, J. Qiu, X. Liu, B. Zheng, Y. Zhao, J. Li, H. He, K. Zhou, Z. Xiao, Q. Li, G. F. Ortiz, Y. Yang, *Energy Storage Mater.* **2020**, *26*, 503.
[38] D. J., Morgan Surface and Interface analysis, **2015**, *47*, 11 https://doi.org/10.1002/sia.5852.
[39] H. Qi, X. Guan, G. Lei, M. Zhao, H. He, K. Li, G. Zhang, F. Zhang, X. Fan, W. Peng, Y. Li, *Nanomaterials.* **2021**, *11*, 1228.
[40] H. Yue, W. Zhang, B. Yu, Y. Hu, Y. Lu, Y. Chen, D. Yang, *J. Mater. Sci.* **2020**, *55*, 11489.
[41] D. Rochefort, P. Dabo, D. Guay, P. M. A. Sherwood, *Electrochim. Acta.* **2003**, *48*, 4245.
[42] C. Schlumberger, C. Scherdel, M. Kriesten, P. Leicht, A. Keilbach, H. Ehmann, P. Kotnik, G. Reichenauer, M. Thommes, *Microporous Mesoporous Mater.* **2022**, *329*, 111554.
[43] Z. Fan, H. Men, *Metals.* **2022**, *12*, 1454.
[44] Y. Wang, H. Li, S. Di, B. Zhai, A. Kelarakis, P. Niu, S. Wang, L. Li, *Carbon Energy.* **2024**, *6*, e388.
[45] H. Hu, C-W. Kao, C. Cheng, X. Xia, Y. Shen, X. Zhou, G. Liu, L. Wang, P. Zeng, J. Mao, T-S. Chan, L. Zhang, *ACS Appl. Mater. Interfaces.* **2023**, *15*, 30332.
[46] M. Tamaru, X. Wang, M. Okubo, A. Yamada, *Electrochem. Commun.* **2013**, *33*, 23.
[47] O. A. González-Meza, E. R. Larios-Durán, A. Gutiérrez-Becerra, N. Casillas, J. I. Escalante, M. Bárcena-Soto González-Meza, *J. Solid State Electrochem.* **2019**, *23*, 3123.
[48] J. Kim, S. Park, S. Hwang, W. Yoon, *J. Electrochem. Sci. Technol.* **2021**, *13*, 19.
[49] J. Wang, J. Kang, Z. Y. Gu, Q. Liang, X. Zhao, X. Wang, R. Guo, H. Yu, C. F. Du, X. L. Wu, *Adv. Funct. Mater.* **2022**, *32*, 2109694.
[50] T. Kim, W. Choi, H. C. Shin, J. Y. Choi, J. M. Kim, M. S. Park, W. S. Yoon, *J. Electrochem. Sci. Technol.* **2020**, *11*, 14.
[51] N. Jiang, Q. Liu, J. Wang, W. Yang, W. Ma, L. Zhang, Z. Peng, Z. Zhang, *Small.* **2021**, *17*, 2007103.
[52] M. Ren, Z. Zhu, Z. Liang, Y. Huang, T. Zhang, M. Hou, K. Zhang, Z. Chen, Y. He, Z. Ma, J. Chen, F. Li, *Small.* **2023**, *19*, 2304187.
[53] H. Xu, J. Zong, X. Liu, *Ionics.* **2018**, *24*, 1939.
[54] C. Marino, E. Marellia, C. Villevieille, *RSC Adv.* **2017**, *23*, 13851.
[55] R. Zhao, J. Zhang, G.-H. Lee, K. Zhang, V. W-H. Lau, J.-J. Lee, I. Moudrakovski, Y.-L. Yang, F. Zou, M. Park, I.-M. Hungg, Y.-M. Kang, *J. Mater. Chem. A.* **2020**, *8*, 12424.
[56] J. Tang, J. Barker, V. G. Pol, *Energy Technol.* **2018**, *6*, 220.
[57] M. Steinhauer, S. Risse, N. Wagner, K. A. Friedrich, *Electrochim. Acta.* **2017**, *228*, 652.
[58] P.-F. Wang, Y. You, Y.-X. Yin, Y.-G. Guo, *Adv. Energy Mater.* **2018**, *8*, 1701912.
[59] M. Islam, M. S. Ahmed, D. Han, G. A. K. M. R. Bari, K.-W. Nam Gels, **2024**, *10*, 24.
[60] A. Langella, A. Massaro, A. B. Muñoz-García, M. Pavone, *Chem. Mater.* **2024**, *36*, 2370.
[61] B. Kalyoncuoglu, M. Ozgul, S. Altundag, E. Altin, I. Moeez, K. Y. Chung, M. Arshad, M. G. Aydin, T. Depci, S. Altin, S. Sahinbay, *ACS Appl. Energy Mater.* **2023**, *6*, 11993.
[62] E. Jeong Kim, T. Hosaka, K. Kubota, R. Tatara, S. Kumakura, S. Komaba, *ACS Appl. Energy Mater.* **2022**, *5*, 12999.
[63] Y. Liu, C. Wang, S. Zhao, L. Zhang, K. Zhang, F. Li, J. Chen, *Chem. Sci.* **2021**, *12*, 1062.
[64] N. Yabuuchi, M. Kajiyama, J. Iwatate, H. Nishikawa, S. Hitomi, R. Okuyama, R. Usui, Y. Yamada, S. Komaba, *Nat. Mater.* **2012**, *11*, 512.
[65] J. Xu, M. Sun, R. Qiao, S. E. Renfrew, L. Ma, T. Wu, S. Hwang, D. Nordlund, D. Su, K. Amine, J. Lu, B. D. McCloskey, W. Yang, W. Tong, *Nat. Commun.* **2018**, *9*, 947.
[66] J. S. Kim, B. H. Kim, D. C. Kim, H. J. Lee, M. G. Kim, A. Maignan, B. Raveau, Y. W. Park, *J. Supercond.* **2004**, *17*, 183.
[67] M. N. Ates, Q. Jial, A. Shah, A. Busnaina, S. Mukerjee, K. M. Abraham, *J. Electrochem. Soc.* **2014**, *161*, 3.
[68] S. Akama, W. Kobayashi, K. Amaha, H. Niwa, H. Nitani, Y. Moritomo, *Sci. Rep.* **2017**, *7*, 43791.
[69] E. Yalman, S. Altundag, M. G. Aydın, Y. Onal, T. Depci, H. Tekbas, F. Bulut, S. Yaşar, S. Altin, *Energy Technol.* **2023**, *11*, 2300014.
[70] B. H. Toby, R. B. Von Dreele, *Powder Diffr.* **2014**, *29*, S2.
[71] S. Altundag, S. Altin, S. Yaşar, E. Altin, *Vacuum.* **2023**, *210*, 111853.
[72] B. Ravel, M. Newville, *Phys. Scr.* **2005**, *T115*, 1007.
[73] G. Kresse, J. Furthmüller, *Comput. Mater. Sci.* **1996**, *6*, 15.
[74] G. Kresse, J. Hafner, *Phys. Rev. B.* **1993**, *47*, 558.
[75] G. Kresse, J. Furthmüller, *Phys. Rev. B.* **1996**, *54*, 11169.
[76] P. E. Blöchl, *Phys. Rev. B.* **1994**, *50*, 17953.
[77] J. P. Perdew, K. Burke, M. Ernzerhof, *Phys. Rev. Lett.* **1996**, *77*, 3865.
[78] L. Wang, T. Maxisch, G. Ceder, *Phys. Rev. B.* **2006**, *73*, 195107.
[79] B. Li, R. Shao, H. Yan, L. An, B. Zhang, H. Wei, J. Ma, D. Xia, X. Han, *Adv. Funct. Mater.* **2016**., *26*, 1330.
[80] K. Okhotnikov, T. Charpentier, S. Cadars, *J. Cheminform.* **2016**, *8*, 17.
[81] A. Y. Toukmaji, J. A. Board, *Comput. Phys. Commun.* **1996**, *95*,73.
[82] S. P. Ong, W. D. Richards, A. Jain, G. Hautier, M. Kocher, S. Cholia, D. Gunter, V. L. Chevrier, K. A. Persson, G. Ceder, *Comput. Mater. Sci.* **2013**, *68*, 314.